Article

Not peer-reviewed version

On the Role of Exposure Time on Al-Si10-Mg Powder Processed by Selective Laser Melting

Paola Leo * , Gilda Renna , Neetesh Soni , Fabio De Pascalis , Teresa Primo , Antonio Del Prete

Posted Date: 10 November 2023

doi: 10.20944/preprints202311.0710.v1

Keywords: Al-Si10-Mg; Selective Laser Melting; exposure time; microstructure; defects; corrosion; hardness

Article

On the Role of Exposure Time on Al-Si10-Mg Powder Processed by Selective Laser Melting

Paola Leo [1,*], Gilda Renna [1], Neetesh Soni [1], Fabio De Pascalis [2], Teresa Primo [1] and Antonio Del Prete [1]

[1] Department of Engineering for Innovation, University of Salento, Via Per Monteroni, 73100 Lecce (LE), Italy;

[2] ENEA - Division for Sustainable Materials, Research Centre of Brindisi, S.S.7 Appia Km 706, 72100 Brindisi, Italy;

* Correspondence: Paola Leo, paola.leo@unisalento.it

Abstract: In this study, the effect of increasing exposure time on microstructures, defectiveness, mechanical properties and corrosion behavior of selective laser melted sample Al-Si10-Mg powder have been investigated. The sample were processed at the same power (375 W) and scan speed (2000 mm/s) but with increasing exposure time. Exposure time equal to 40, 50 and 60 μs was applied. The features of the analyzed samples show that with increasing exposure time a better efficiency of the heat input has been obtained, with larger size of melting pool and Si particles and lower defectiveness. Moreover, being the coarser microstructure associated a to lower level of voids, the average hardness is similar for the analyzed samples. The potentiodynamic curves of the samples show that the voids occurrence is more significant with respect to the scale of microstructure on corrosion behavior being the sample processed at the highest exposure time the more resistant to corrosion. The experimental techniques used in the present study were Optical Microscope (OM), Scanning Electron Microscope (SEM), hardness and X-Ray Computed Tomography.

Keywords: Al-Si10-Mg; Selective Laser Melting; exposure time; microstructure; defects; corrosion; hardness

1. Introduction

Al-Si10-Mg alloy is widely used for casting due to the near-eutectic composition. The role of Mg in the alloys is to increases hardness both by solid solution or aging treatment [1,2]. The main applications of Al-Si10-Mg alloys are in the fields of aerospace and automobiles due to the high strength-to-weight ratio, to their low density, high specific strength, good corrosion resistance. Those alloys exhibit also excellent electric and thermal conductivity [1–5].

Selective Laser Melting (SLM) is a 3D printing technology that uses a high-energy laser beam to completely melt a layer of powder in a protective atmosphere along the laser path [4,5]. Successive layers are added to the previous ones and on each layer, the laser path melts the powder according to the required geometry of the component and guarantee a bonding with the previous layer. So, at the end of the building process, a three-dimensional component is formed "layer by layer" or with additive method. With respect to traditional subtractive manufacturing method, SLM can produce more complex geometry with reduced waste of material [6,7].

When processed by SLM, Al-Si10-Mg alloy exhibits a very fine microstructure respect the traditional casting process, due to the high cooling rate involved in the process. Moreover, the high thermal gradient lead mainly to a cellular microstructure [8–11]. That cellular microstructure is mainly Al solid solution supersaturated by alloying atoms because of the high cooling rate that limit particles precipitation and is mixed with Al-Si eutectic phase at the grain boundary [12]. This fine microstructure guarantees high strength and toughness.

 doi:10.20944/preprints202311.0710.v1

Anyway, SLM parts suffer from relatively low surface quality and voids occurrence [13,14] that reduce the fatigue strength (bypassing the initial stage of microcrack nucleation) [15–18] and the corrosion resistance [19]. Regarding the defectiveness, gaps between adjacent scanning tracks has been observed for Al-Si10-Mg when hatch scan space increased to 150 μm and beyond [20]. Also scan speed and scan strategies and laser volumetric energy density (VED) strongly affect porosity evolution [21].

The energy density received by metallic powder can be expressed by Equation (1) according to [22], where P is the laser power [W], v is the scanning speed [mm/s], h is the hatch spacing [mm], and lt is the layer thickness [mm].

$$VED=P/v\cdot h\cdot lt \quad (1)$$

But if the laser beam works with pulses spaced of a certain point distance (Pd, distance points) and exposure time (Et, exposure time), the scanning speed can be also expressed as the ratio between the Pd [mm] and the Et [s] so the VED can be even expressed also as in equation (2) [23]:

$$VED= P\cdot Pd/ Et\cdot h\cdot lt \quad (2)$$

So, the same value of VED can be obtained by combining properly Pd and Et.

The role of exposure time on microstructure evolution and defect has been investigated by the authors in a previous study [12] showing that very close values of energy density (70,175.4 J/mm^3 and 70,707.1 J/mm^3) do not lead to very similar microstructures, defects and mechanical properties if the Et is changed. So, in this paper the authors intend detail the previous results isolating the role of the Et on microstructure and defects of Al-Si10-Mg parts produced at constant Energy Density. For the Al-Si10-Mg parts processed at the same VED, the exposition time (Et) parameter has shown to be effective in modifying the microstructure and quality of the samples. Consequently, the properties of the parts can be controlled with minor modifications of the process parameters.

2. Materials and Methods

The composition of the gas-atomized powder of an average diameter equal to 40 μm is shown in Table 1. Cube samples (10 mm edge) were built along Z axe (Figure 1) with Meander strategy using a Renishaw AM 400 machine.

Table 1. Powder composition (wt.%).

Si	Fe	Cu	Mn	Mg	Cr	Zn	Ti	Al
0,80	0,40	0,10	0,50	1,2	0,30	0,20	<0,15	bal.

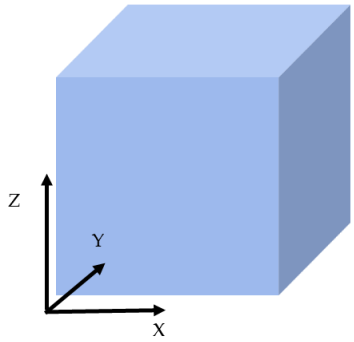

Figure 1. Building direction of the Al-Si10-Mg cube sample (Z).

After processing, a stress relief treatment (300 °C for 2 h) was applied. Three samples were built for each set of process parameters. As shown in Table 2, all the samples were processed at the same power (375 W) and scan speed (2000 mm/s) but with increasing exposure time. To better recall the

Preprints (www.preprints.org) | NOT PEER-REVIEWED | Posted: 10 November 2023 doi:10.20944/preprints202311.0710.v1

samples process parameters during the analysis, the samples were named with S followed by t1, t2, or t3 suffixes according to the increasing exposure time (respectively) 40, 50 and 60 μs.

Table 2. Samples designation and SLM process parameters.

Samples	Power (W)	Exposure Time (μs)	TOFF (μs)	Point Distance (μm)	Hatch Distance (mm)	Layer Thickness (mm)	DEV (j/mm³)	v (mm/s)	E Line (J/mm)
St1	375	40	20	120	0,09	0,03	69444,4	2000	0,1875
St2	375	50	20	140	0,09	0,03	69444,4	2000	0,1875
St3	375	60	20	160	0,09	0,03	69444,4	2000	0,1875

Optical microscope and scanning electron microscope were used for investigating the microstructure. Particularly, NIKON Ephiphot 200 OM and ZEISS EVO SEM equipped with a Bruker energy-dispersive X-ray spectrometer (EDX) was employed.

For the optical microscope microstructure analysis, after metallographic preparative, the longitudinal (L) and transversal (T) sections of the samples were etched using Keller etching (95 mL water, 2.5 mL HNO_3, 1.5 mL HCl, 1.0 mL HF). On the L sections of the cubic specimens, the average depth and width of the melt pools were evaluated using NIS Nikon software for image analysis, supplied with optical microscope. All the welding pools in the L sections were characterized. SEM analyses supported by ImageJ software, was mainly focused to evaluate the amount and size of the Silicon particles as a function of the different process parameters and post processing heat treatment.

The samples were also analysed by X-ray microtomography. This technique allows for the non-destructive investigation of their internal structure, and it's useful for void and porosity analysis [24]. The computed tomographic (CT) system used is a GE Phoenix "nanotom s" present in the ENEA Research Centre laboratory at Brindisi (Italy). This instrument is equipped with a high-performance nano-focus X-ray tube (180 kV/15 W) and a tungsten transmission target. The analysis was performed setting the acquisition parameters of the instrument as reported in Table 3. The size of the analysed cuboid-shaped samples is shown in Table 4. Figure 2 shows three orthogonal tomographic sections and the 3D virtual reconstruction related to the sample St1.

Table 3. CT experimental conditions.

Target	Voltage (KV)	Current (μA)	Integration Time (ms)	Voxel size (μm)	Number of radiographies
Tungsten	100	100	500	8	2000

Table 4. Geometry of the samples analysed by CT.

Sample	Edge Size	Volume (mm3)
St1	≈ 10x10x3.7 mm³	360.17 mm³
St2	≈ 10x10x5.6 mm³	560.23 mm³
St3	≈10x10x3.85 mm³	383.40 mm³

Preprints (www.preprints.org) | NOT PEER-REVIEWED | Posted: 10 November 2023 doi:10.20944/preprints202311.0710.v1

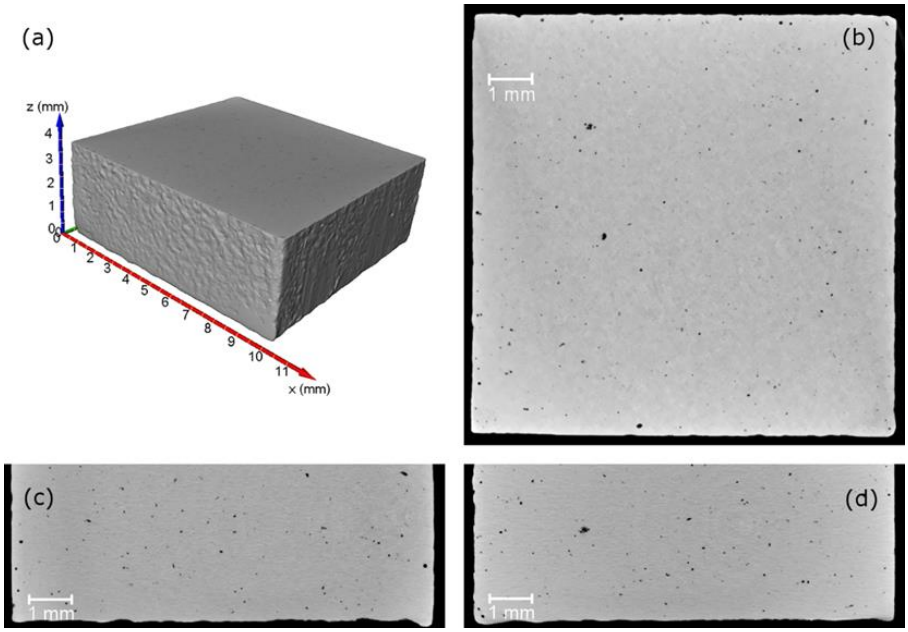

Figure 2. Sample St1; 3D virtual reconstruction (a) and XY (b), XZ (c) and YZ (d) sections.

Observing the tomographic sections, the presence of small pores within the samples is evident. To identify and measure them, an automatic segmentation procedure based on the Bernsen's algorithm [25,26] and well described by F. H. Kim et al. [27] was applied. Figure 3 shows a 3D reconstruction of the specimen St1 where the pores are highlighted in red. For each pore, the volume, the equivalent diameter, and the sphericity were calculated.

For a given particle, the equivalent diameter is defined as the diameter of the spherical particle of the same volume. So, the equivalent diameter is given by the following formula:

$$EqD = \left(6V / \pi\right)^{1/3} \tag{3}$$

whilst the sphericity represents a shape indicator expressed such as:

$$Sph = \frac{\pi^{1/3}(6V)^{2/3}}{A} \tag{4}$$

where V is the volume of a particle and A is its surface area. Sphericity ranges from 0 to 1 (sphere). As suggested by Kim et al [27] only pores larger than 125 voxels in volume were used for the spherical analysis.

Once the pores were detected, porosity was calculated as the ratio between the sum of their volumes and the total volume of the sample. In the pores volume evaluation, to avoid the pixel noise contribution, pores with volume less than $4.09*10^{-6}$ mm^3 (2x2x2 voxels) were excluded [28].

Vickers hardness was measured using a Affri Wiky 200JS digital instrument employing 0.1 Kg. for holding time equal to 15 s ($HV_{0.1/15}$), according to Vickers Hardness ISO 6507-1 (2018) standard. Average hardness values were calculated from edge-to-edge indentation in perpendicular direction, cutting the center of the section. The distance between indentations was equal to 100 μm on T and L sections.

The corrosion resistance of the as-built samples was evaluated using Gamry Potentiostat 1010E. The measurements were carried out in an aqueous solution of 3.5% NaCl at room temperature, with naturally aerated, near-neutral conditions. A standard three-electrode cell configuration was used, consisting of a graphite as expanded mesh counter electrode, an Ag/AgCl reference electrode, and the samples as the working electrode. All potentials were referenced to Ag/AgCl. To ensure accurate measurements, the samples were insulated using Teflon and electric connection by copper wire with soldering, covering their cut edges and back sides, leaving only a 1.0 cm^2 surface area exposed to the electrolyte. The steady-state potential was determined after immersing the samples in the solution at

Preprints (www.preprints.org) | NOT PEER-REVIEWED | Posted: 10 November 2023 doi:10.20944/preprints202311.0710.v1

open circuit potential (OCP) for 15 minutes. Subsequently, potentiodynamic polarization measurements were performed, scanning from -2 V to 0,5 V vs Ag/AgCl at a scan rate of $2mVs^{-1}$.

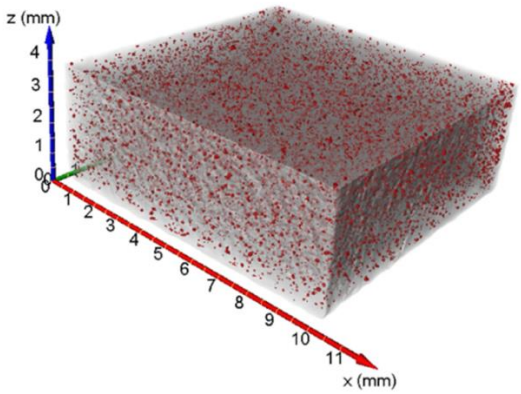

Figure 3. 3D transparent view of the porosity analysis for St1 sample.

3. Results and Discussion

3.1. Microstructure Characterization

The microstructure of the samples by optical microscope is shown in Figure 4 where micrographs taken from the center of T (XY) and L (YZ) sections are shown. In particular Figure 4 a,c,e show the microstructural features of T sections and Figure 4 b,d,f those ones of longitudinal sections.

In both the sections, the boundaries of the melting pool are well highlighted by chemical etching. In the T sections, adjacent elongated tracks can be observed sometime interrupted by circular zone due to the remelting of the track by laser action on the next layer. In the L section the cup shape of the melting pool is also clearly highlighted. That near hemispherical shape gives information on heat transfer mode that should occur mainly by conduction and so being governed by Rosenthal equation of the heat flow [22]. All the samples exhibit common microstructures features that characterize the boundaries of the melting pool and their inner parts. In Figure 5 the same portion of a melting pool boundary is highlighted by the red circles and has been observed at different magnification. As the magnification increases (Figure 5 b,c) the heterogeneity of microstructure between the boundary and the inner part can be observed. Two main aspects are evident from optical analysis:

1. The boundary microstructure is coarser respect to the inner part of the melting pool.
2. The morphology is less elongated (more equiaxed) in the boundary respect to the inner part where appears mainly cellular.

The less elongate zone at the boundary of the melting pool could be generated by the partial remelting of the cellular microstructure in the previous layer. Indeed, the partial remelting broke the original cellular structure forming a more equiaxed morphology that is also coarse due to the overheating of the zone [23,29]. On the contrary, the completely fused powder that characterize the inner of the melting pool space grow cellular due to the high thermal gradient that characterize the SLM process, and moreover the favorite growth direction is the 1 0 0 crystallographic direction because of the crystalline cubic system of the Aluminum [22]. Regarding the compositional features of the solidifying alloy, the first materials that solidify is a solid solution (α-Al phase). While the last solidified alloy, characterized by the lower melting temperature is the eutectic phase. Usually, due to the fast cooling rate, the α-Al phase remain supersaturated till room temperature but, according to different process parameters also secondary particles can precipitate from the supersaturated α-Al.

Preprints (www.preprints.org) | NOT PEER-REVIEWED | Posted: 10 November 2023 doi:10.20944/preprints202311.0710.v1

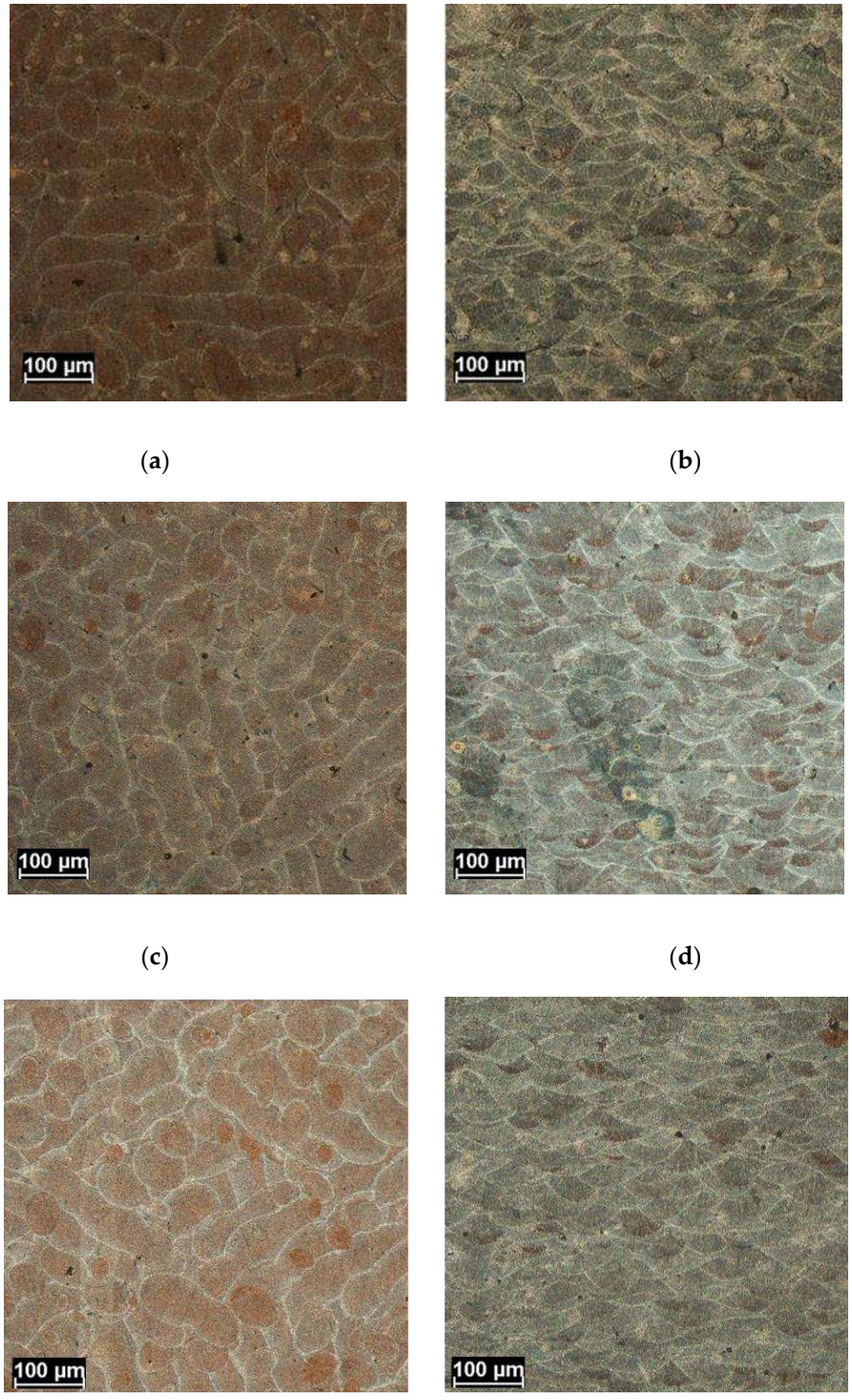

Figure 4. Optical microscope microstructure for St1 (a,b), St2 (c,d) and St3 (e,f) as results in the T(a,c,e) and L (b,d,f) sections.

 doi:10.20944/preprints202311.0710.v1

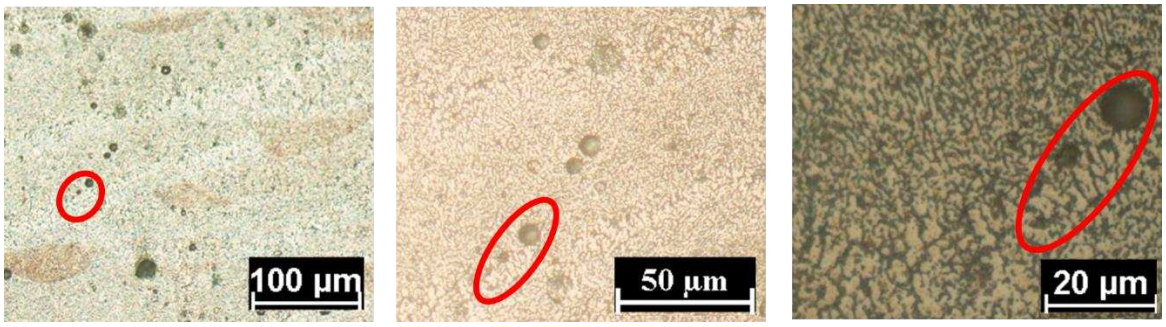

(a) **(b)** **(c)**

Figure 5. Solidification morphology at the same boundary (red circle) and inside the melting pool evaluated at increasing magnification: a (100X), b (500X) and c(1000X).

Figure 6 show the microstructure of the three samples close to a melting point boundary (in the red shape). The main secondary phase (white particles) is Silicium particles as expected and also verified from many previous study [1,2,29] while the gray phase is the Al solid solution. The first observation is that, according to the microstructure analysis, the boundary non cellular microstructure seems to extend as the exposure time increases. Moreover, in Figure 7, micrographs of the samples processed at the extreme exposure time (St1 and St3) close to melting pool boundaries are compared at high magnification. Higher grain size in St3 sample can be observed as the exposure time is increased. Moreover, a different distribution of the second phases particles seems to occur in the samples. Samples St1 should have a higher amount of small fine particles that also are more uniformly distributed in the matrix. This last aspect can be observed also in Figure 6 despite the lower magnification.

To verify the role of the exposition time on the microstructure and therefore to validate the qualitatively consideration suggested from the analysis of Figure 6 and Figure 7, the average size of melting pool have been evaluated on the L sections as well as the average width of the track in the T sections. The hypothesis of the authors is that with increasing exposure time, the energy losses are reduced and so, even if the VED is constant, the effective heat input is higher as exposure time increases.

The result of the analysis is shown in Table 5. Table 5 shows that at constant VED, the size of the melting pool is increased with the exposure time being slightly higher in the St3 sample. So, the actual heat input is increased with exposure time and according to the Rosenthal equation of heat flow, the cooling rate is decreases making the microstructure coarser as results from the Figures 6 and 7.

During the heat treatment at 300°C-2h the metastable as built systems move towards a more equilibrium state through rejection of Silicon from the supersaturated matrix (leading to heterogeneous precipitation of Silicon particles), and fragmentation of continuous eutectic silicon network with subsequent spheroidization [30–32]. As the heat treatment time further increases, the Si particles becomes coarser. Finally, Ostwald effect induce a decreasing in number of the smaller particles and an increasing in size of the largest ones [31,32]. Indeed, Ostwald repining effect leads to further reduction of Gibbs free energy by reduction of the energy surface of the particles. The smaller particles dissolve in the matrix and the dissolved atoms increase the size of the biggest ones leading to a more equilibrium state of the sample.

Comparing St1 and St3 samples (Figures 6 and 7), a higher density of small particle size in St1 sample can be qualitatively observed. That observation has been confirmed by Image J analysis of the particles density (Table 6) and size distributions (Figure 8). The particles density is reduced from 11,1 to 8,6 (N/ µm^2) from St1 to St3 samples (Table 6) that is characterized by a lower occurrence of smaller particles (Feret's diameter lower than 0.6 µm in Figure 8) and higher amount of the coarsest ones (diameter higher than 1.10 µm).

Preprints (www.preprints.org) | NOT PEER-REVIEWED | Posted: 10 November 2023 doi:10.20944/preprints202311.0710.v1

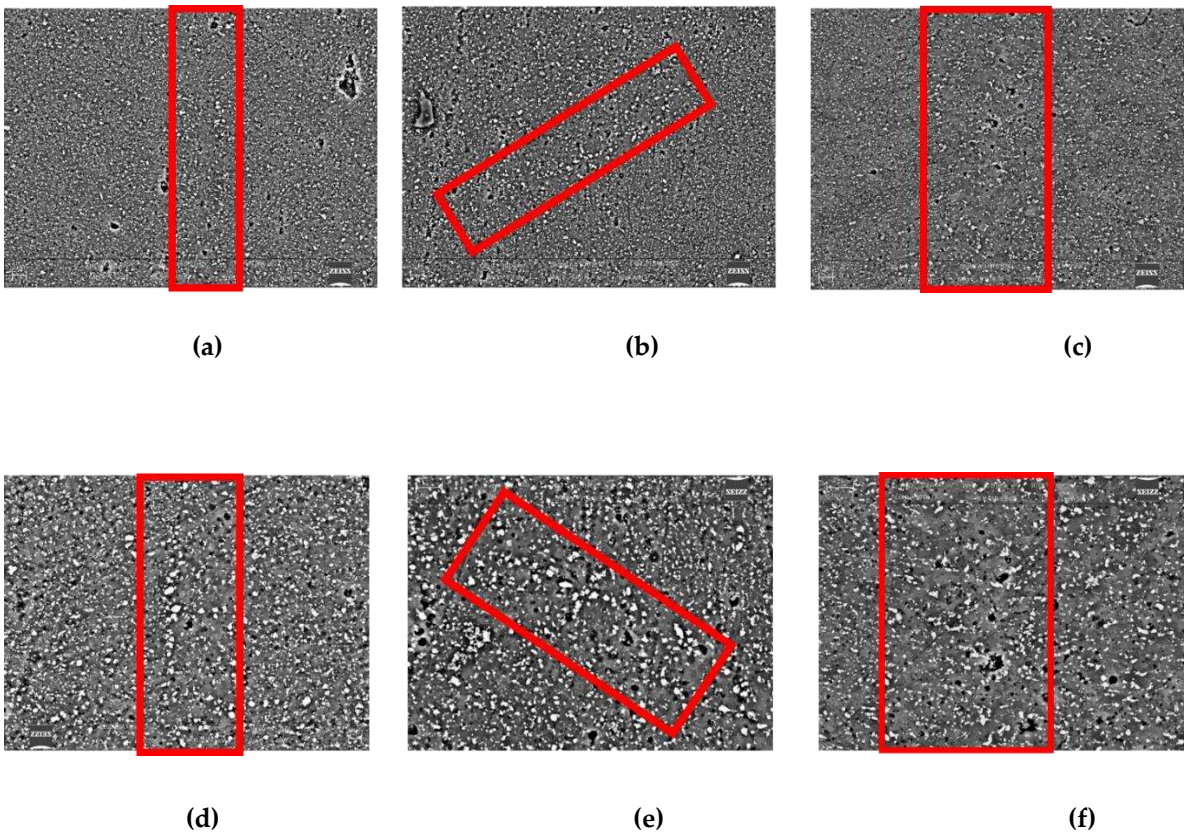

Figure 6. SEM microstructure of microstructure for St1 (a,d), St2 (b,e) and St3 (c,f) where the red shape enclose a melting pool boundary at 5K (a,b,c) and 10K (d,e,f) magnification.

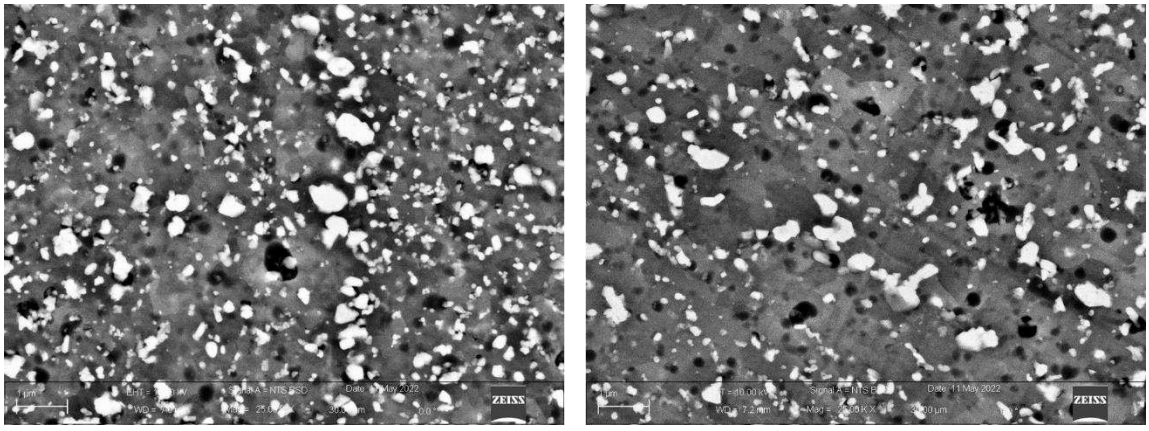

Figure 7. High magnification SEM microstructure of St1 (a), and St3 (b) samples close to a melting pool boundary. The grains are much more visible in St3 samples. Moreover, a lower amount of small particles in St3 sample is evident.

Preprints (www.preprints.org) | NOT PEER-REVIEWED | Posted: 10 November 2023 doi:10.20944/preprints202311.0710.v1

Table 5. Size of the melting pool in L and T sections.

Sample	Width of Melting pool L section (XZ) (no edge)	Depth of Melting Pool L section (XZ) (no edge)	Track Width T section (XY) (no edge)
St1	132±17	50±6	87±6
St2	142±20	76±5	87±3
St3	157±12	74±8	92±1

Table 6. Particles density in St1 e St3 samples.

Sample	Si particles density (Total Number/μm^2)
St1	11,1
St3	8,6

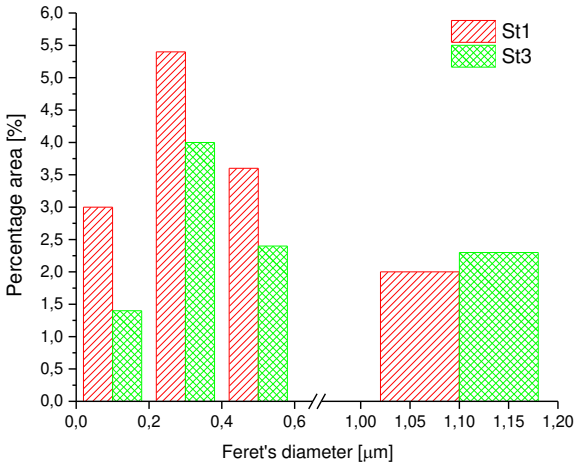

Figure 8. Size distribution of Silicon particles in St1 and St3 samples.

The higher density (Table 6) and smaller size of the Si particles (Figure 8) in St1 samples could be due to the fine microstructure of St1 together with its high matrix supersaturation that favors the breaking up of the eutectic phases during the heat treatment. In fact, eutectic fragmentation is promoted by Si interdiffusion through Aluminum matrix and therefore by the higher matrix supersaturation of St1 samples leading to a small, distributed fragment. Moreover, also the average size of the eutectic phase decreases with the size of the microstructure speeding up the fragmentation and spheroidization process. [33].

Coarser particles (Feret's diameter higher than 0,6 μm) occur for both the samples at the melting pool boundaries (Figures 6 and 7). Differently from the inner of the melting pool, during the building process the melting pool boundaries are interested by remelting and overheating as discussed previously (Figure 5) and the original cellular structure is changed in coarser equiaxed grain and eutectic Si phase [34–36] (Figures 5-7). So, the higher heat input in St3 sample lead to a more effective coarsening at the melting pool boundary and upon the 300°C-2h heat treatment the Si particles remain coarser for the St3 sample. Moreover, Ostwald repining effect (that means more elongated and widely spaced particles) [33,37] is much more evident close to grain boundaries (Figure 6 and 7) because of the overheating that start to fragment the Si phase already during the building process [34–36] and so, with the post-processing heat treatment, the eutectic evolution goes to completion with the dissolution of the smaller particles and the growing of the bigger ones. The lowest density of the smaller particles in the St3 sample could be also show that the completion of the eutectic

Preprints (www.preprints.org) | NOT PEER-REVIEWED | Posted: 10 November 2023 doi:10.20944/preprints202311.0710.v1

evolution by Orowan mechanism is favored by the higher heat input and more efficient fragmentation during the building process. Anyway, further study is required to clarify this last aspect.

3.2. Defectiveness and hardness

The results of the X-ray microtomography analysis including the value of porosity for each specimen are reported in Table 6. In all the observed samples, the voids are characterized by a spherical shape (the average sphericity is around 0.9) and by an equivalent mean diameter in the range of 35 -39μm being minimum for St3 sample. The porosity measured for sample St3 is 0.18%, while for the samples St1 and St2 it is around 0.37% and 0.33% respectively. So, as the efficiency of the heat increases due to the increasing of the exposure time, also the number per unit volume, the size and so the average volume of the pores is decreased. While the exposure time does not affect significant the morphology of the porosity that is mainly spherical.

Table 6. Porosity Characterization.

Sample	Pores Number	Porosity %	Equivalent diameter (μm)	Volume (mm^3)	Sphericity
St1	28627	0.372	Average:38.50 range: 19.85-181.25	Average: $4.69*10^{-5}$ range:$4.10*10^{-6}$ – $3.12*10^{-3}$	Average: 0.864 range: 0.351-1.0
St2	38490	0.327	Average:38.85 range: 19.85-176.05	Average: $4.75*10^{-5}$ range:$4.10*10^{-6}$ – $2.86*10^{-3}$	Average: 0.906 range: 0.297-1.0
St3	19605	0.181	Average:34.84 range: 19.85-152.22	Average: $3.53*10^{-5}$ range:$4.10*10^{-6}$ – $1.85*10^{-3}$	Average: 0.906 range: 0.331-1.0

Considering the distribution of the equivalent diameter of the samples (Figure 10) is observable that the pores occurring in highest number are also characterized by the smallest equivalent diameter (approximately lower than 35/40 μm). For the bigger pores, the occurrence decreases with the equivalent diameter but more sharply in the case of St3. So the effect of the highest exposure time is most evident on the reduction of the amount of higher size pores while is not significant for pores of equivalent diameter lower than 35/40 μm.

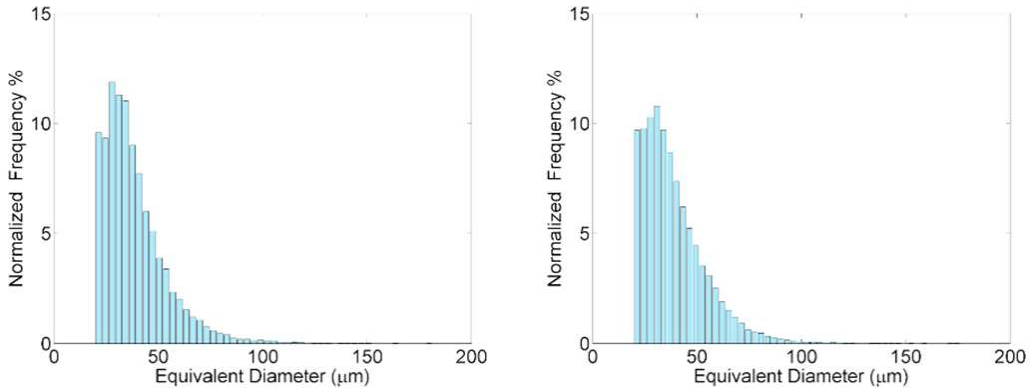

(**a**) (**b**)

Preprints (www.preprints.org) | NOT PEER-REVIEWED | Posted: 10 November 2023 doi:10.20944/preprints202311.0710.v1

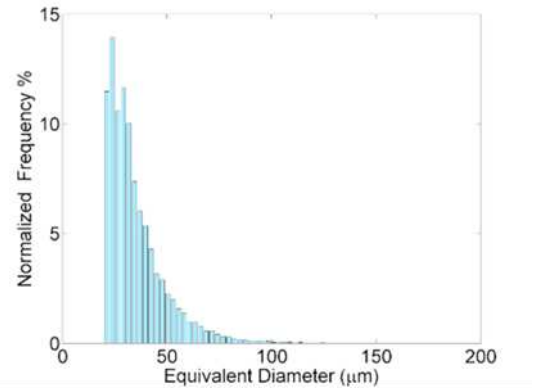

(c)

Figure 10. Distribution of the equivalent diameter of the pores of St1 (a), St2 (b) and St3 (c) samples.

Furthermore, the local variation of the porosity along the X, Y and Z axes was studied (Figures, 11-12). The graphs were obtained by measuring the level of porosity on each individual slice, like a virtual sectioning of the sample with 8 μm thick slices along the three orthogonal directions. The graphs show that the pores are uniformly distributed inside the volume of the specimens, except for the regions adjacent to the lateral faces where a greater presence of defects was revealed (see initial and final peaks in the variation of porosity along X and Y. In Figure 11, the edges of the XY surface of St1, St2 and St3 (without chemical etching) has been reconstructed for giving evidence of the greater amount of defectiveness at the edge respect to the porosity amount close to a half of X edge and Y edge in the inner of the section. This phenomenon is due to the variation of scan speed near the edge that lead to deeper melting pool and also favour gas/ vapor entrapplement as shown in [12]. Along the build direction (Z) each slice gets the average value of different XY plane and so porosity value fluctuates around the average value as shown in Figure 12

The microhardness values are similar for all the investigated samples as shown in Table 7. The coarser microstructure of St3 samples should lead to a lower hardness respect to St1 and St3 samples but St3 sample is also characterized by the lowest amount of porosity that therefore counterbalances the less hardening microstructure.

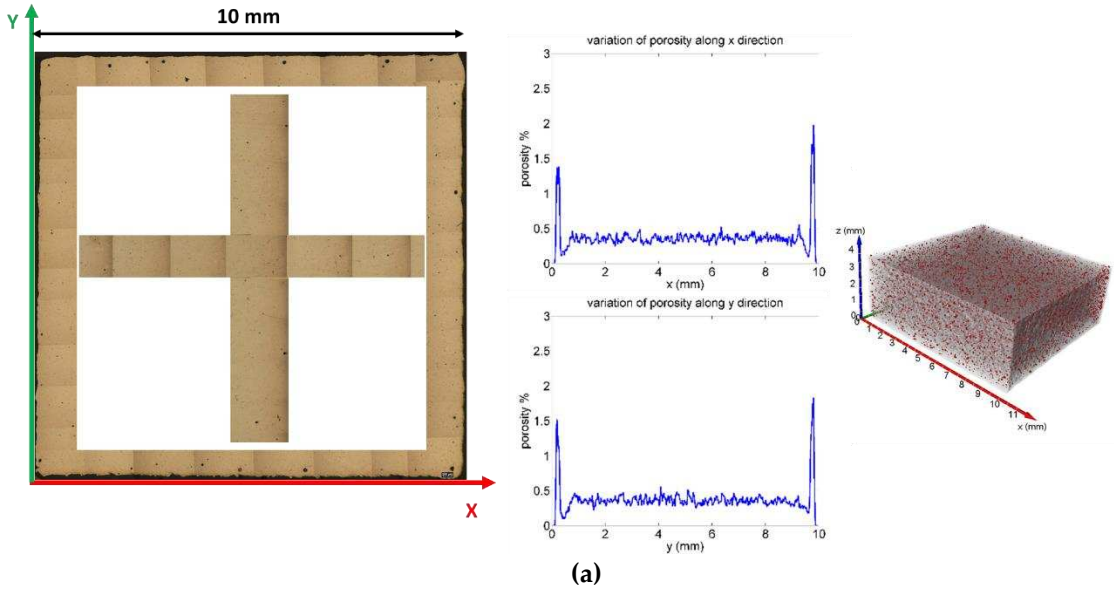

(a)

Preprints (www.preprints.org) | NOT PEER-REVIEWED | Posted: 10 November 2023 doi:10.20944/preprints202311.0710.v1

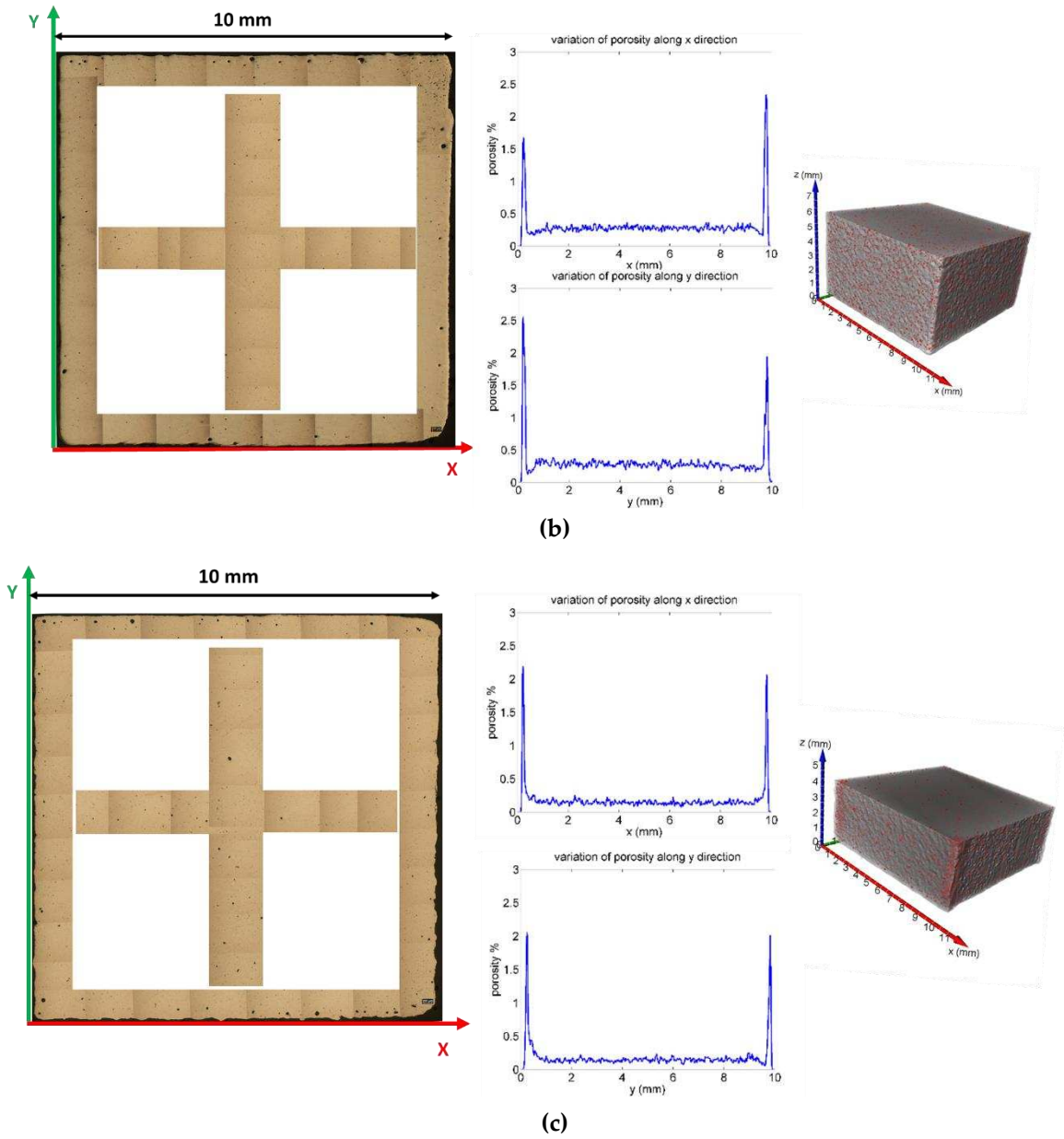

Figure 11. Porosity distribution along X and Y axes for St1 (a), St2 (b) and St3 samples. It has been also shown the distribution of porosity as results from optical microscope analysis along the edge of the external X-Y surface and at and half of X edge and Y edge.

Preprints (www.preprints.org) | NOT PEER-REVIEWED | Posted: 10 November 2023 doi:10.20944/preprints202311.0710.v1

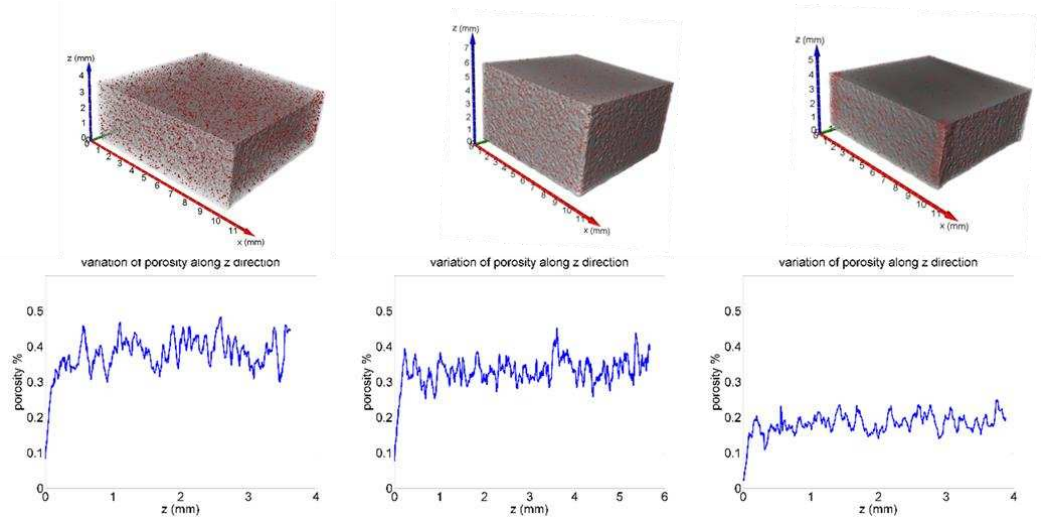

(a) **(b)** **(c)**

Figure 12. Porosity distribution along Z axe for St1 (a), St2 (b) and St3 samples (c).

Table 7. Average microhardness in the longitudinal (XZ) and transversal (XY) section.

Sample	HV 0.1/15 L section (XZ) (no edge)	HV 0.1/15 T section (XY) (no edge)
St1	71±1	71±1
St2	70±1	71±1
St3	70±0	70±0

3.3. Corrosion Behavior

In Table 8 is shown the open circuit potential (OCP). The corresponding potentiodynamic polarization curves are shown in Figure 13 while in Figure 14 the optical micrographs of the corroded surfaces are shown. The analysis of the potentiodynamic curves indicates that the corrosion current (ICorr) decreases at the highest exposure time improving the sample corrosion resistance. In particular, the ICorr values are closer for St1 and St2 samples while decreases for St3 sample. The analysis of the OCP shows that the samples are characterized by very proxime values. Those similar values of OCP highlight similar features of the native oxide layers on all samples [38,39]. Anyway, the less noble OCP value (more negative) was found for St1 and St2 samples sample indicating a slightly lower electrochemical stability and higher activity of its surface. This could possibly be due to a less uniform microstructure and compositional inhomogeneity between the core and the boundaries of the melting pool or to a higher volume of porosity [40]. According to the previous analysis of the samples, it has been shown that finer microstructure together with smaller size and more uniform distribution of Si particles have been found in St1 and St2 samples even if associated with a higher defectiveness level. So, the slightly less noble OCP values for those samples seem to be much more affected by the voids amount respect to the microstructure and silicon particles scale. The same phenomenon could be also responsible for the higher ICorr of St1 and St2 samples respect to St3 as shown in Figure 14.

Table 8. OCP values for St1, St2 and St3 samples.

Sample	OCP [V]
St1-T	-0,772±0,001
St2-T	-0,772±0,001
St3-T	-0,761±0,003

Preprints (www.preprints.org) | NOT PEER-REVIEWED | Posted: 10 November 2023 doi:10.20944/preprints202311.0710.v1

In fact, according to literature [37] the corrosion rate of Aluminum alloys improves with decreasing grain size. The improved resistance is due to an ability of high grain boundary density surfaces to passivate more readily. Moreover, as shown by [40] coarser Si precipitates result in a higher potential difference between the Si and Al matrix favoring the corrosion process.

As a consequence, the more refined microstructure of St1 and St2 samples should lead to both higher passive layer stability and increased corrosion resistance [40–42]. But St1 and St2 show higher values of corrosion current, respect to the St3 sample. So, the higher amount of porosity in the finer microstructure samples (St1 and St2) overcome the positive effect of the microstructure on corrosion behavior leading to poor corrosion resistance respect to St3. Evidence of results shown in Figure 13, are given in Figure 14 a, b, c where optical micrographs of the exposed surface of the samples after potentiodynamic test are shown. The most corroded samples are indeed St1 and St2, confirming the role of porosity on corrosion behavior.

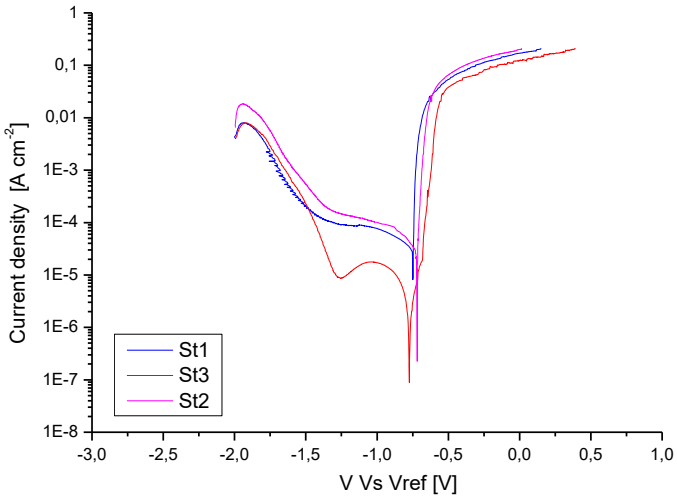

Figure 13. Potentiodynamic curves for St1, St2 and St3 samples showing a nobler corrosion behavior for St3 sample.

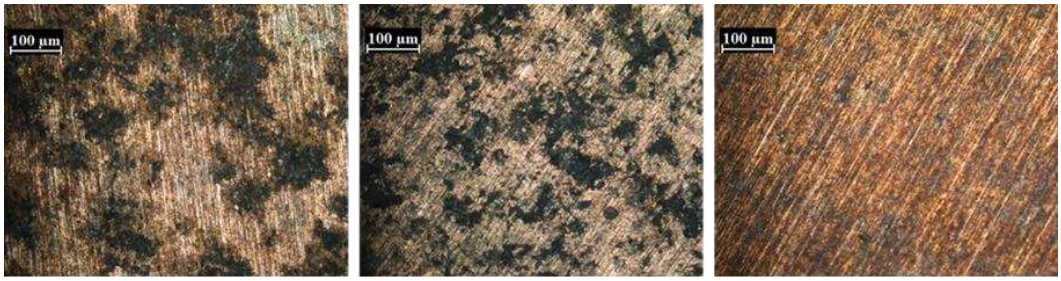

Figure 14. Optical micrographs of the exposed surface after the corrosion test for St1 (a), St2 (b) and St3 (c) samples.

4. Conclusion

In this study the authors have shown that with increasing of the exposure time on Al-Si10-Mg powder processed by Selective Laser Melting at the same laser power (375W), speed (2000mm/s) and scanning strategy the resulting microstructure and properties change as in the following:

1. The melting pool size increases with exposure time that reduces the energy loss and lead to higher efficiency of the energy input.

 doi:10.20944/preprints202311.0710.v1

2. After stress relief heat treatment, the density of Si particles decreases and the average size increases with exposure time.

3. As the efficiency of the heat increases due to the increasing of the exposure time, also the number, the size and so the average volume of the voids is decreased.

4. Due to the opposite effect of exposure time on voids occurrence and microstructure scale, the hardness values do not change with exposure time.

5. The corrosion resistance increases with exposure time, despite the coarser melting pool size and Si particles, showing that corrosion behavior in the analyzed samples is much more sensitive to the void occurrence than to the microstructural features.

Author Contributions: Conceptualization, P.L. G.R. T.P and A.D; formal analysis, P.L.; investigation, P.L., G.R, F.D.P, N.S; data curation, P.L; writing—original draft preparation, P.L.; writing—review and editing all the Authors; visualization, P.L.; supervision, P.L.; validation, P.L. All authors have read and agreed to the published version of the manuscript.

Funding: This work has been supported by Ministry of Economic Development, Bando Horizon 2020 - PON 2014/2020, Innovative Solutions for the quality and sustainability of ADDitive manufacturing processes – SIADD project.

Acknowledgments: The authors thank very much the HB-Technology company of Taranto (Italy) for their support.

Conflicts of Interest: The authors declare no conflict of interest.

References

1. Polmear, I.J. *Light Alloys-Metallurgy of the Light Metals*, 3rd ed.; Arnold: London, UK, 1995; pp. 169-180.
2. Smith, W.F. *Structure and Properties of Engineering Alloys*, 2nd ed.; McGraw-Hill: London, UK, 1993; pp. 218-223
3. Asphal, Y.; Jawalkar, C.S.;Kant, S. A review on use of aluminium alloys in aircraft components, *J. Mater. Sci.*, **2015**, 3, pp. 33-38.
4. Praneeth J.; Venkatesh, S; Krishna L.S. Process parameters influence on mechanical properties of AlSi10Mg by SLM, *Mater. Today: Proc. (in press)* 2023, https://doi.org/10.1016/j.matpr.2022.12.222
5. Brandl, E.; Heckenberger, U.; Holzinger, V.; Buchbinder, D. Additive manufactured AlSi10Mg samples using Selective Laser Melting (SLM): Microstructure, high cycle fatigue, and fracture behavior. *Mater. Des.* **2012**, 34, pp 159-169
6. 6. Zhang, J.; Song, B.; Wei, Q.; Bourell, D.; Shi, Y. A review of selective laser melting of aluminum alloys: Processing, microstructure, property and developing trends. *J. Mater. Sci. Technol.* **2019**, 35, pp. 270–284.
7. Aboulkhair, N.T.; Simonelli, M.; Parry, L.; Ashcroft, I.; Tuck, C. 3D printing of Aluminium alloys: Additive Manufacturing of Aluminium alloys using selective laser melting. *Prog. Mater. Sci.* **2019**, 106, 100578, pp.1-45
8. Aboulkhair, N.T.; Maskery, I.; Tuck, C.; Ashcroft, I.; Everitt, N.M. On the formation of AlSi10mg single tracks and layers in selective laser melting: microstructure and nano-mechanical properties, *J. Mater. Process. Technol.* **2016**, 230, pp. 88–98.
9. Yadroitsev, I.; Krakhmalev, I. P.;. Yadroitsava, S.J; Smurov, I. Energy input effect on morphology and microstructure of selective laser melting single track from metallic powder, *J. Mater. Process. Technol.* **2013,** 213 (4) pp. 606–613. 10.1080/17452759.2015.1110868
10. Lam, L.P; Zhang,D.Q.; Liu, Z.H.; Chua, C.K. Phase analysis and microstructure characterisation of AlSi10Mg parts produced by selective laser melting, *Virtual Phys. Prototyp.* **2015**, 10, pp. 207–215
11. Liu, Y.J.; Liu, Z.; Jiang, Y.; Wang, G.W.; Yang, Y.; Zhang, L.C. Gradient in microstructure and mechanical property of selective laser melted AlSi10Mg, *J. Alloys Compd.* **2018**, 735, pp. 1414–1421, https://doi.org/10.1016/ j.jallcom.2017.11.020.
12. Leo, P.; Del Prete, A.; Primo, T.; Nacucchi, M. Al-Si10-Mg Manufactured by Selective Laser Melting: Microstructure Sensitivity to Close Values of the Heat Input, *Metals* **2023**, 13, 590. https://doi.org/ 10.3390/met13030590

13. Maskery, I.; Aboulkhair , N.T.; Corfield , M.R.; Tuck, C.; Clare, A.T. ; Leach, R.K. ; Wildman, R.D. ; Ashcroft , I.A.; Hague, R.J.M. Quantification and characterisation of porosity in selectively laser melted Al–Si10–Mg using X-ray computed tomography, *Mater. Charact*. **2016** 111, pp.193–204.
14. Patel, D.; Pandey, A. Powder bed fusion of aluminium alloys: A review of experimental explorations – Microstructure, mechanical properties, and recent advances *Mater. Today: Proc*. **2023,** 82, pp. 168–177
15. Miller, K. The short crack problem. *Fatigue Fract. Eng. Mater. Struct.* **1982**, 5, pp.223–232.
16. Schijve, J. *Fatigue of structures and materials*. Springer, 2d ed, 2009, pp. 13-21
17. Takahashi, K.; Murakami, Y. Quantitative evaluation of effect of surface roughness on fatigue strength. *Engineering against fatigue.* Benyon. J.; Brown, M.; Smith, R.; Lindley, T.; Tomkins, B; editors. Balkema Publishers, 1999, pp-693-703
18. Suraratchai, M.; Limido, J.; Mabru, C.; Chieragatti, R. Modelling the influence of machined surface roughness on the fatigue life of aluminium alloy. *Int. J. Fatigue*, **2008**, 30, pp. 2119–26.
19. Leon,A.; Aghion, E. Effect of surface roughness on corrosion performance of AlSi10Mg alloy produced by Selective Laser Melting (SLM), *Mat. Charact.* **2017**, 131, pp. 188–194.
20. Aboulkhair, N.T; Everitt,N.M; Ashcroft, I.; Tuck, C. Reducing porosity in AlSi10Mg parts processed by selective laser melting, *Addit. Manuf. 1*, **2014**, pp. 77–86.
21. Haboudou, A.; Peyre, P.; Vannes, A.B.; Peix, G. Reduction of porosity content generated during Nd: YAG laser welding of A356 and AA5083 aluminium alloys, *Mater. Sci. Eng. A*, **2003**, 363 (1–2), pp. 40–52.
22. Messler, R.W., Jr. *Principles of Welding: Processes, Physics, Chemistry, and Metallurgy;* Wiley: New York, NY, USA, 1999
23. Wang, L-Z.; Wang, S.; Wu, J. Experimental investigation on densification behavior and surface roughness of AlSi10Mg powders produced by selective laser melting. *Opt. Laser Technol.* **2017**, 96, pp. 88–96
24. Du Plessis, A.; Yadroitsev, I.; Yadroitsava, I.; Le Roux, S.G. X-Ray microcomputed tomography in additive manufacturing: a review of the current technology and applications, *3D Print. Addit. Manuf.* **2018**, pp.227-247, http://doi.org/10.1089/3dp.2018.0060
25. Bernsen, J. Dynamic thresholding of grey-level images. International conference on pattern recognition, Paris, France, 1986, pp. 1251-1255.
26. Sankur, B. Survey over image thresholding techniques and quantitative performance evaluation. *J. Electron. Imaging*, **2004,** 13(1), 146. doi:10.1117/1.1631315
27. Kim, F.H.; Moylan, S.P.; Garboczi, E.J.; Slotwinski J.A. Investigation of pore structure in cobalt chrome additively manufactured parts using X-ray computed tomography and three-dimensional image analysis. *Addit. Manuf.*, **2017**,17, pp.23-38; https://doi.org/10.1016/j.addma.2017.06.011
28. Du Plessis,A.; Sperling, P.; Beerlink, A.; Tshabalala, L.; Hoosain, S.; Mathe, N.;. le Roux, S.G. Standard method for microCT-based additive manufacturing quality control 1: Porosity analysis, *MethodsX*, **2018,** 5, pp.1336-1345, https://doi:10.1016/j.mex.2018.09.005
29. Wu,L.; Zhao,Z.; Bai, P.; Zhang, Z.; Li,Y.; Liang, M.; Du W. The Effect of Silicon Phase Morphology on Microstructure and Properties of AlSi10Mg Alloys Fabricated by Selective Laser Melting, *Materials*, **2022**, 15, 8786, https://doi.org/10.3390/ma15248786
30. Fiocchi, J.; Tuissi, A.; Bassani, P.; Biffi, C.A. Low temperature annealing dedicated to AlSi10Mg selective laser melting products, *J. Alloys Compd.*, **2017**, 217, pp. 3402-3409
31.] Wei, L.; Shuai, L.; Jie, L. Effect of heat treatment on AlSi10Mg alloy fabricated by selective laser melting: Microstructure evolution, mechanical properties and fracture mechanism. *Mater. Sci. Eng. A*, **2016**, 663, pp. 116–125.
32. Li, X.P.; Wang, X.J.; Saunders, M. A selective laser melting and solution heat treatment refined Al–12Si alloy with a controllable ultrafine eutectic microstructure and 25% tensile ductility. *Acta Mater.* **2015**, 95, pp. 74–82
33. Ogris, E.; Wahlen, A.; Luchinger, H.; Uggowitzer, P.J. On the silicon spheroidization in Al–Si alloys. *J. Light Met.* **2002**, 2, pp. 263–269
34. Liu, X.; Zhao, C.; Zhou, X.; Shena, Z.; Liu, W. Microstructure of selective laser melted AlSi10Mg alloy. *Mater. Des*. **2019**, 168, 107677.
35. Patakham, U.; Palasay, A.; Wila, P.; Tongsri, R.; MPB characteristics and Si morphologies on mechanical properties and fracture behavior of SLM AlSi10Mg, *Mater. Sci. Eng*., **2021,** A 821, 141602
36. Wanga, L.Z.; Wanga, S.; Hongb, X.; Pulsed SLM-manufactured AlSi10Mg alloy: Mechanical properties and microstructural effects of designed laser energy densities, *J. Manuf. Process*., **2018**, 35, pp.492-499
37. Ibrahim, M.; Abdelaziz , M.; Samuel , A.; Doty, H.; Samuel, F.; Spheroidization and Coarsening of Eutectic Si Particles in Al-Si-Based Alloys, *Adv. Mater. Sci. Eng.* **2021**, Article ID 6678280, https://doi.org/10.1155/2021/6678280

38. Rafieazad,M.; Mohammadi, M.; Gerlich, A.; Nasiri, A. Enhancing the corrosion properties of additively manufactured AlSi10Mg using friction stir processing, *Corros. Sci.*, **2021**,178, 109073
39. Rafieazad,M.; Chatterjee, A.; Nasiri A.M. Effects of Recycled Powder on Solidification Defects, Microstructure, and Corrosion Properties of DMLS Fabricated AlSi10Mg. *JOM*, **2019**, https://doi.org/10.1007/s11837-019-03552-2
40. Rafieazad,M.; Mohammad, M.; Nasiri, A.M. On microstructure and early stage corrosion performance of heat treated direct metal laser sintered AlSi10Mg. *Addit. Manuf.* **2019**, 28, pp. 107–119
41. Ralston, K.D.; Birbilis, N.; Davies, C.H.J. Revealing the relationship between grain size and corrosion rate of metals, *Scr. Mater*. **2010**, 63, pp. 1201–1204, https://doi. org/10.1016/j.scriptamat.2010.08.035.
42. Rao, A.G.; Katkar, V.A.; Gunasekaran, G.; Deshmukh, V.P.; Prabhu, N.; Kashyap, B.P. Effect of multipass friction stir processing on corrosion resistance of hypereutectic Al–30Si alloy, *Corros. Sci.*, **2014** 83, pp.198–208 https://doi.org/10.1016/j. corsci.2014.02.013.